

## Parity-violating photon circular polarization in $p + d \rightarrow {}^3\text{He} + \gamma$ with pion-less effective field theory

H. Nematollahi,<sup>\*</sup> S. Bayegan,<sup>†</sup> N. Mahboubi,<sup>‡</sup> and M. Moeini Arani<sup>§</sup>

*Department of Physics, University of Tehran, Tehran, Iran*



(Received 18 June 2017; revised manuscript received 17 October 2017; published 12 January 2018)

The nonleptonic weak interaction in the few-nucleon system at very low energies is studied with the calculation of the photon circular polarization in the  $pd \rightarrow {}^3\text{He}\gamma$  reaction ( $P_\gamma^{pd}$ ). For very low energies, one may treat the pion as heavy and integrate it out from the QCD symmetry-based model-independent effective field theory, leaving only short-range strong interactions which are introduced in term of pionless effective field theory formulation. We investigate a complete set of the parity-violating electromagnetic transitions in the  $pd \rightarrow {}^3\text{He}\gamma$  process. In this paper the interferences of strong, electromagnetic, Coulomb, and parity-violating weak interactions are presented with the calculation of a full set of appropriate diagrams at the leading order. We have obtained energy-dependent  $P_\gamma^{pd}$  results as a function of the laboratory energy values  $0.5 \leq E_{\text{Lab}} \leq 3$  MeV in terms of the low-energy coupling constants. The contributions of the initial  $S$ - and  $P$ -wave proton-deuteron systems have been considered to make the final  ${}^3\text{He}$  ground state in this energy region.

DOI: [10.1103/PhysRevC.97.014001](https://doi.org/10.1103/PhysRevC.97.014001)

### I. INTRODUCTION

The analysis of purely leptonic and semileptonic weak interaction in isolation are well understood. However in the nucleus, the effects of nonperturbative strong interactions between quarks from those generated by the weak interaction cannot be disentangled [1]. At low energies, lattice QCD or effective field theories have been suggested to pursue the problem leading to preliminary rigorous predictions.

The parity-violating (PV) observable in heavy nuclei is most probably the result of weak interactions among only two or three constituent nucleons and this physics cannot presently be studied because of the complicated strong interaction physics involved. Therefore, the goal of independent measurements and theoretical efforts is to constrain the nonleptonic weak interaction in the few-body systems. At very low energies the model-independent pionless effective field theory [EFT( $\mathcal{T}$ )], that systematically incorporates the symmetries of QCD, provides the powerful theory to understand the physics of strong, electromagnetic [2–4], and Coulomb interactions in a consistent manner [5,6] for the few-body system. Further, the symmetries of standard model at the leading order (LO) introduce nucleon-nucleon ( $NN$ ) PV Lagrangian with five PV low-energy constants (LECs) that parametrize the weak interaction physics in terms of nucleon degree of freedom [7]. We intend to use the model-independent EFT( $\mathcal{T}$ ) approach to disentangle nonperturbative strong interactions from those generated by the weak interaction in the few-body systems such as  ${}^3\text{He}$  and reliably produce the nonleptonic weak interaction observable.

In the present paper, we calculate photon circular polarization in the  $pd \rightarrow {}^3\text{He}\gamma$  process,  $P_\gamma^{pd}$ , with the EFT( $\mathcal{T}$ ) approach at LO. The parity-conserving (PC) [5] and PV amplitudes of the  $pd \rightarrow {}^3\text{He}\gamma$  process are presented with the incoming proton energies which are limited by the perturbative treatment of Coulomb effects and the EFT( $\mathcal{T}$ ) breakdown scale. In the laboratory energy range  $E_{\text{Lab}} \geq 0.5$  MeV the initial  ${}^2S_{\frac{1}{2}}$  and  ${}^4S_{\frac{3}{2}}$  channels of the proton-deuteron system can be converted to the final  ${}^2S_{\frac{1}{2}}$  state of the  ${}^3\text{He}$  nucleus using the appropriate combinations of the  $E1$  and PV interactions. Also, the mixing of the  $M1$  and PV interactions can change the initial  ${}^2P_{\frac{1}{2}}$ ,  ${}^2P_{\frac{3}{2}}$ ,  ${}^4P_{\frac{1}{2}}$ , and  ${}^4P_{\frac{3}{2}}$  states of the proton-deuteron system to the final  ${}^3\text{He}$  ground state. The electromagnetic (EM) transitions can amplify the observable  $P_\gamma^{pd}$  with all the PV-EM transitions and its reversed combinations e.g.,  ${}^2S_{\frac{1}{2}} \xrightarrow{\text{PV}} {}^2P_{\frac{1}{2}} \xrightarrow{E1} {}^2S_{\frac{1}{2}}$  or  ${}^4P_{\frac{3}{2}} \xrightarrow{M1} {}^4P_{\frac{1}{2}} \xrightarrow{\text{PV}} {}^2S_{\frac{1}{2}}$ . In the presence of the Coulomb interaction, we show that the PV effect is modified due to the diagrams connecting the different PV two-body transitions and Coulomb interaction. To obtain the well-converged results we have extrapolated our results to  $\lambda$  (mass of the photon)  $\rightarrow 0$ . We use the full set of complicated LO diagrams consisting of simultaneous interferences among weak, strong short-range, Coulomb long-range, and electromagnetic interactions to evaluate the  $P_\gamma^{pd}$ . We calculate the photon circular polarization observable as a function of laboratory energy with three different cutoff momentums: 400, 600, and 900 MeV. Theoretical uncertainty for our results is provided with the cutoff variation of  $P_\gamma^{pd}$  between 400 and 900 MeV, which indicates no significant cutoff dependence in the final values.

The values of PV LECs are not fixed by the symmetries of QCD but must be constrained by future measurements. The lack of five experimental measurements for PV observables is the main obstacle to pin down the five PV coupling constants

<sup>\*</sup>hnematollahi.91@ut.ac.ir

<sup>†</sup>Corresponding author: bayegan@ut.ac.ir

<sup>‡</sup>n.mahboubi@ut.ac.ir

<sup>§</sup>m.moeini.a@ut.ac.ir

of LO Lagrangian. The PV asymmetries such as the polarized photon induced process on the triton or  $^3\text{He}$  at, e.g., an upgraded HIGS facility (HIGS2) [8] and new measurement at HIGS2 for the photo-induced PV asymmetries on the deuteron [8] to the desired precision of  $10^{-8}$  would provide more independent determinations of the PV LECs.

The structure of our paper is as follows. We present the effective Lagrangian for the  $pd \rightarrow ^3\text{He}\gamma$  process in Sec. II. PV formalism for the  $pd$  scattering is introduced in Sec. III. Section IV discusses the derivation of the PV amplitude for the  $pd \rightarrow ^3\text{He}\gamma$  reaction. The numerical calculation and the results of the photon circular polarization  $P_\gamma^{pd}$  are also presented in Sec. V. Finally, we summarize the paper in Sec. VI.

## II. EFFECTIVE LAGRANGIAN FOR THE PV $pd \rightarrow ^3\text{He}\gamma$ PROCESS

The effective Lagrangian for the PV  $pd$  capture reaction can be classified as the PC:  $\mathcal{L}_{\text{PC}}$  and PV:  $\mathcal{L}_{\text{PV}}$  sectors

$$\mathcal{L} = \mathcal{L}_{\text{PC}} + \mathcal{L}_{\text{PV}}. \quad (1)$$

The  $\mathcal{L}_{\text{PC}}$  contains the strong ( $\mathcal{L}_s$ ), Coulomb ( $\mathcal{L}_{\text{ph}}$ ), and electromagnetic ( $\mathcal{L}_{\text{EM}}$ ) interactions,

$$\mathcal{L}_{\text{PC}} = \mathcal{L}_s + \mathcal{L}_{\text{ph}} + \mathcal{L}_{\text{EM}}, \quad (2)$$

that are introduced in detail in the following.

### A. Strong interaction

The strong interaction in the  $pd$  system using the EFT( $\mathcal{T}$ ) formalism based on dibaryon auxiliary fields is given by the Lagrangian [9,10]

$$\begin{aligned} \mathcal{L}_s = & N^\dagger \left( iD_0 + \frac{\vec{D}^2}{2m_N} \right) N + d_s^{A\dagger} \left[ \Delta_s - c_{0s} \left( iD_0 + \frac{\vec{D}^2}{4m_N} + \frac{\gamma_s^2}{m_N} \right) \right] d_s^A \\ & + d_t^{i\dagger} \left[ \Delta_t - c_{0t} \left( iD_0 + \frac{\vec{D}^2}{4m_N} + \frac{\gamma_t^2}{m_N} \right) \right] d_t^i - (y_s d_s^{A\dagger} (N^\dagger P^A N) + y_t d_t^{i\dagger} (N^\dagger P^i N) + \text{H.c.}) \\ & + \frac{m_N H(E, \Lambda)}{6} N^\dagger (y_t^2 (d_t^i \sigma_i)^\dagger (d_t^j \sigma_j) - [y_t y_s (d_t^i \sigma_i)^\dagger (d_s^A \sigma_A) + \text{H.c.}] + y_s^2 (d_s^A \tau_A)^\dagger (d_s^B \sigma_B)) N + \dots, \end{aligned} \quad (3)$$

where  $D_\mu$  is the covariant derivative which acts on the nucleon ( $N$ ) and dibaryon fields ( $d_t^i$  and  $d_s^A$ ) with the  $\partial_\mu + ie\frac{1+\tau_3}{2}A_\mu$  and  $\partial_\mu + ieCA_\mu$  relations, respectively.  $A_\mu$  and  $e$  are the external field and the electron charge. We have  $C = 2, 1$ , and  $0$  for the proton-proton, proton-neutron, and neutron-neutron dibaryons.  $m_N$  represents the nucleon mass and  $y_{t,s}^2 = \frac{8\pi}{m_N^2 \rho_{t,s}}$  are two PC coupling constants for the singlet and triplet channels with the effective ranges  $\rho_{t,s}$ . The parameters  $\Delta_{s/t}$  and  $c_{0s/t}$  are given by matching the EFT( $\mathcal{T}$ )  $NN$ -scattering amplitude to the effective range expansion (ERE) of the scattering amplitude of two nonrelativistic nucleons around the  $i\gamma_{s/t}$ , where  $\gamma_t = 45.702$  MeV is the binding momentum of the deuteron and  $\gamma_s = \frac{1}{a_s}$  with  $a_s$  as the singlet scattering length.

The operators

$$P^i = \frac{1}{\sqrt{8}} \sigma_2 \sigma^i \tau_2, \quad P^A = \frac{1}{\sqrt{8}} \sigma_2 \tau_2 \tau^A, \quad (4)$$

with  $\tau_A$  ( $\sigma_i$ ) as isospin (spin) Pauli matrices, project the  $NN$  system to the  $^3S_1$  and  $^1S_0$  states, respectively. The three-nucleon force is also introduced by  $H(E, \Lambda)$ , where  $E$  and  $\Lambda$  denote the total energy and the cutoff momentum.

### B. Coulomb interaction

The Coulomb contribution which is dominant for small momentum transfers enters  $\sim \frac{\alpha m_N}{p}$  where  $p$  is the momentum transfer and  $\alpha$  denotes the fine structure constant [11–14]. With

respect to the Coulomb potential

$$V_c = \frac{\alpha}{p^2}, \quad (5)$$

one cannot assume that the scale of all momenta is set by the deuteron binding momentum  $\gamma_t$  and we have to introduce a new momentum scale  $p$ , where  $p \ll Q$  for the power counting [13]. Thus, we simultaneously have an effective theory with two small expansion parameters  $\frac{Q}{\Lambda}$  and  $\frac{p}{\alpha m_N}$ .

The Lagrangian of the kinetic and gauge fixing terms of the photons is

$$\begin{aligned} \mathcal{L}_{\text{ph}} = & -\frac{1}{4} F_{\mu\nu} F^{\mu\nu} - \frac{1}{2\xi} (\partial_\mu A^\mu - \eta_\mu \eta_\nu \partial^\nu A^\mu)^2, \\ \eta_\mu = & \text{timelike unit vector.} \end{aligned} \quad (6)$$

Therefore the static photon propagator is given by

$$i\Delta_{\text{ph}}(p) = \frac{i}{p^2 + \lambda^2}, \quad (7)$$

where the infrared divergences in the photon propagator will be handled by inserting a photon mass  $\lambda$ . The final results are obtained using an extrapolation when  $\lambda \rightarrow 0$ . In fact, by choosing a mesh-point distribution dense around the Coulomb peak, it is possible to numerically take the zero-screening limit  $\lambda$  [11]. We work in the region  $E_{\text{Lab}} \geq 0.5$  MeV, so the Coulomb parameter  $\frac{\alpha m_N}{p}$  is of order  $\frac{1}{3}$  and nonperturbative treatment of Coulomb effects is not necessary.

### C. Electromagnetic interaction

The  $E1$ ,  $M1$ , and  $E2$  transitions contribute to the  $pd \rightarrow {}^3\text{He}\gamma$  amplitude at the low-energy regime. With respect to the experimental facts for the  $pd \rightarrow {}^3\text{He}\gamma$  reaction [15,16], the contribution of the  $E2$  transition is small compare to the  $M1$  transition at the low energy. We introduce the EM interaction as

$$\mathcal{L}_{\text{EM}} = \mathcal{L}_E + \mathcal{L}_B, \quad (8)$$

where at the leading order, the electric interaction of a photon with a single nucleon is introduced by the Lagrangian

$$\mathcal{L}_E = \frac{e}{2m_N} N^\dagger \left( \frac{1 + \tau_3}{2} \right) (\vec{P} + \vec{P}') \cdot \vec{\varepsilon}_\gamma^* N, \quad (9)$$

with  $\vec{P}$  and  $\vec{P}'$  as the momenta for the incoming and outgoing nucleons. Also,  $\vec{\varepsilon}_\gamma$  denotes the three-vector polarization of the produced photon.

Also, the Lagrangian of the  $M1$  interaction is constructed by considering the nucleon and dibaryon operators coupling to the magnetic field  $\vec{B}$ ,

$$\begin{aligned} \mathcal{L}_B = & \frac{e}{2m_N} N^\dagger (k_0 + k_1 \tau^3) \vec{\sigma} \cdot \vec{B} N + \frac{eL_1}{m_N \sqrt{\rho_t \rho_s}} d_t^{j\dagger} d_s^j B_j \\ & - \frac{2eL_2}{m_N \rho_t} i \varepsilon_{ijk} d_t^{i\dagger} d_t^j B_k + \text{H.c.}, \end{aligned} \quad (10)$$

where  $k_0 = \frac{1}{2}(k_p + k_n) = 0.4399$  and  $k_1 = \frac{1}{2}(k_p - k_n) = 2.35294$ .  $k_p$  ( $k_n$ ) denotes the proton (neutron) magnetic moment. The coefficients  $L_1 = -4.427 \pm 0.015$  fm and  $L_2 = -0.4$  fm, which have been fixed using the cross section of the  $np \rightarrow d\gamma$  at thermal energy and the deuteron magnetic moment  $\mu_M$ , enter at next-to-leading order (NLO) [17]. So only the first term of Eq. (10) is sufficient for our leading-order calculations.

### D. Leading-order PV interaction

The PV interaction connects the states with the different parity and the same total angular momentum. So at the lowest order for the PV interaction, we have  ${}^3S_1 \rightarrow {}^1P_1$ ,  ${}^3S_1 \rightarrow {}^3P_1$ , and  ${}^1S_0 \rightarrow {}^3P_0$  two-body transitions. Therefore, the leading-order two-body PV Lagrangian with dibaryon formalism can be written as

$$\begin{aligned} \mathcal{L}_{\text{PV}} = & -[g^{3S_1-1P_1} d_t^{i\dagger} N^T i (\overleftarrow{\nabla} \sigma_2 \tau_2 - \sigma_2 \tau_2 \overrightarrow{\nabla})_i N \\ & + g_{\Delta I=0}^{1S_0-3P_0} d_s^{A\dagger} N^T i (\overleftarrow{\nabla} \sigma_2 \sigma_i \tau_2 \tau_A - \sigma_2 \sigma_i \tau_2 \tau_A \overrightarrow{\nabla})_i N \end{aligned}$$

$$\begin{aligned} & + g_{\Delta I=1}^{1S_0-3P_0} \varepsilon^{3AB} d_s^{A\dagger} N^T (\overleftarrow{\nabla} \sigma_2 \sigma_i \tau_2 \tau_B - \sigma_2 \sigma_i \tau_2 \tau_B \overrightarrow{\nabla})_i N \\ & + g_{\Delta I=2}^{1S_0-3P_0} \mathcal{I}^{AB} d_s^{A\dagger} N^T i (\overleftarrow{\nabla} \sigma_2 \sigma_i \tau_2 \tau_B - \sigma_2 \sigma_i \tau_2 \tau_B \overrightarrow{\nabla})_i N \\ & + g^{3S_1-3P_1} \varepsilon^{ijk} d_t^{i\dagger} N^T (\overleftarrow{\nabla} \sigma_2 \sigma_k \tau_2 \tau_3 - \sigma_2 \sigma_k \tau_2 \tau_3 \overrightarrow{\nabla})_j N \\ & + \text{H.c.} + \dots \end{aligned} \quad (11)$$

where  $\mathcal{I} = \text{diag}(1, 1, -2)$  is a diagonal matrix in isospin space and  $g^{(\bar{x}-\bar{y})}$  denotes the weak dibaryon-nucleon-nucleon ( $dNN$ ) coupling constant for the PV two-body transitions between  $\bar{x}$  ( ${}^3S_1, {}^1S_0$ ) and  $\bar{y}$  ( ${}^1P_1, {}^3P_0, {}^3P_1$ ) partial waves.  $\Delta I$  represents the isospin changing in the PV vertex. To simplify, we use the notation suggested in Ref. [4] in which  $g^{3S_1-1P_1}$ ,  $g_{\Delta I=0}^{1S_0-3P_0}$ ,  $g_{\Delta I=1}^{1S_0-3P_0}$ ,  $g_{\Delta I=2}^{1S_0-3P_0}$ , and  $g^{3S_1-3P_1}$  have been replaced by  $g_1, g_2, g_3, g_4$ , and  $g_5$ , respectively. We note that the  $g_4$  corresponding to the  $g_{\Delta I=2}^{1S_0-3P_0}$  term dose not contribute in the  $pd$  system because of isospin values of the proton and deuteron.

### III. PV $pd$ SCATTERING AMPLITUDE

We introduce one of the major building block of the PV  $pd \rightarrow {}^3\text{He}\gamma$  transition, namely the PV  $pd$  scattering in this section. All LO diagrams of the PV  $pd$  scattering are shown in Fig. 1. In this figure the circle with a cross indicates the possible two-body PV transitions

$${}^3S_1 \leftrightarrow {}^1P_1, \quad {}^3S_1 \leftrightarrow {}^3P_1, \quad {}^1S_0 \leftrightarrow {}^3P_0, \quad (12)$$

which mix the  $S$ - and  $P$ -wave channels at the lowest order. The dashed rectangle and dashed oval also represent the PV- and PC-scattering amplitudes, respectively. For the three-nucleon system, the possible lowest-order transitions which change the parity and conserve the total angular momentum are

$$\begin{aligned} & {}^2S_{\frac{1}{2}} \leftrightarrow {}^2P_{\frac{1}{2}}, \quad {}^2S_{\frac{1}{2}} \leftrightarrow {}^4P_{\frac{1}{2}}, \\ & {}^4S_{\frac{3}{2}} \leftrightarrow {}^2P_{\frac{3}{2}}, \quad {}^4S_{\frac{3}{2}} \leftrightarrow {}^4P_{\frac{3}{2}}. \end{aligned} \quad (13)$$

We emphasize that the three-body  $S$  states  ${}^2S_{\frac{1}{2}}$  and  ${}^4S_{\frac{3}{2}}$  are introduced by  $X$ , and  $Y$  is assigned as the symbol of the  ${}^2P_{\frac{1}{2}}$ ,  ${}^2P_{\frac{3}{2}}$ ,  ${}^4P_{\frac{1}{2}}$ , and  ${}^4P_{\frac{3}{2}}$  channels.

In the cluster-configuration space, the contribution of the diagrams in Fig. 1 can be written as [18]

$$\begin{aligned} t^{\text{LO,PV}}(X/Y \rightarrow Y/X; E, k, p) = & A^{\text{PV}}[X/Y \rightarrow Y/X; E, k, p] \\ & - \frac{1}{2\pi^2} \int_0^\Lambda dq q^2 \left\{ A^{\text{PV}}[X/Y \rightarrow Y/X; E, q, p] \mathcal{D}^{(\text{LO})} \left( E - \frac{q^2}{2m_N}, q \right) t^{\text{LO,PC}}(X/Y; E, k, q) \right. \\ & \left. + t^{\text{LO,PC}}(Y/X; E, q, p) \mathcal{D}^{(\text{LO})} \left( E - \frac{q^2}{2m_N}, q \right) A^{\text{PV}}[X/Y \rightarrow Y/X; E, k, q] \right\} \\ & + \frac{1}{4\pi^4} \int_0^\Lambda dq_1 q_1^2 \int_0^\Lambda dq_2 q_2^2 \left\{ t^{\text{LO,PC}}(Y/X; E, q_2, p) \mathcal{D}^{(\text{LO})} \left( E - \frac{q_2^2}{2m_N}, q_2 \right) \right. \\ & \left. \times A^{\text{PV}}[X/Y \rightarrow Y/X; E, q_1, q_2] \mathcal{D}^{(\text{LO})} \left( E - \frac{q_1^2}{2m_N}, q_1 \right) t^{\text{LO,PC}}(X/Y; E, k, q_1) \right\}, \end{aligned} \quad (14)$$

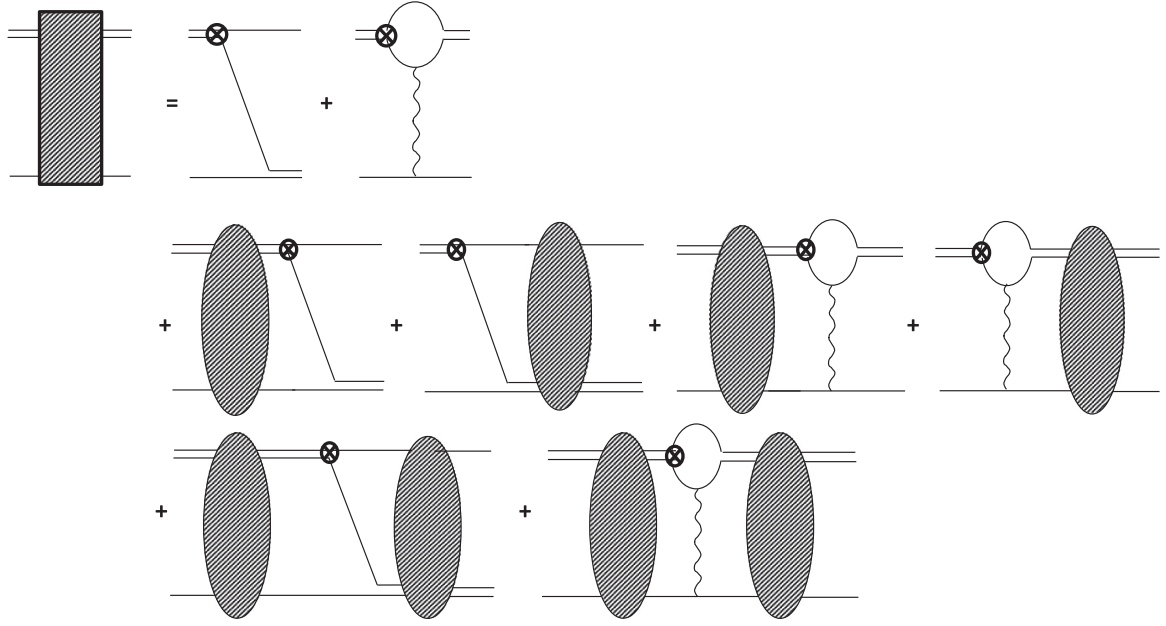


FIG. 1. The PV-scattering diagrams at LO. A single line represents a nucleon and a double line is a dibaryon propagator. The wavy line denotes the exchanged photon. The circle denotes the PV  $dNN$  vertex. A dashed oval indicates the PC-scattering amplitudes at LO. The dashed rectangular represents the PV-scattering amplitude. Time-reversed diagrams are not displayed.

where  $A^{\text{PV}}$  represents the contributions of the PV kernels in the first row of Fig. 1. We can present the function  $A^{\text{PV}}[X/Y \rightarrow Y/X; E, k, p]$  as

$$A^{\text{PV}}[X/Y \rightarrow Y/X; E, k, p] = \sum_{i=1}^4 A_i^{\text{PV}}[X/Y \rightarrow Y/X; E, k, p], \quad (15)$$

where the  $A_1^{\text{PV}}$  and  $A_2^{\text{PV}}$  kernels are for the contributions of the first and second diagrams in the first row of Fig. 1. Moreover, the time-reversed amplitudes of these diagrams (not shown in Fig. 1) are introduced by  $A_3^{\text{PV}}$  and  $A_4^{\text{PV}}$ , respectively. The  $A_{1,2}^{\text{PV}}$ ,  $A_{3,4}^{\text{PV}}$  functions for all possible transitions in the  $J = \frac{1}{2}$  and  $\frac{3}{2}$  channels have been evaluated in Ref. [18].

In Eq. (14), the second term denotes the contribution of the diagrams which include one PC-scattering amplitude, and the third term corresponds to the diagrams in the third line with the scatterings in both sides.  $t^{\text{LO,PC}}(X/Y; E, k, p)$  is the LO PC  $pd$ -scattering amplitude in the  $X/Y$  channel, where  $X = {}^2S_{\frac{1}{2}}, {}^4S_{\frac{3}{2}}$ , and  $Y = {}^2P_{\frac{1}{2}}, {}^2P_{\frac{3}{2}}, {}^4P_{\frac{1}{2}}, {}^4P_{\frac{3}{2}}$ . The LO PC-scattering amplitudes are given using [5]

$$t_q^{(L)}(E, k, p) = \begin{bmatrix} t_{q,t \rightarrow t}^{(L)}(E, k, p) & 0 & 0 \\ 0 & 0 & 0 \\ 0 & 0 & 0 \end{bmatrix}, \quad (16)$$

with

$$t_{q,t \rightarrow t}^{(L)}(E, k, p) = -2y_{tt} \left[ K_s^{(L)}(E, k, p) - \frac{1}{2} K_c^{(L, \text{PC})}(E, k, p) \right] + \frac{y_{tt}}{\pi^2} \int_0^\Lambda dq q^2 \left[ K_s^{(L)}(E, q, p) - \frac{1}{2} K_c^{(L, \text{PC})}(E, q, p) \right] D_t^{(\text{LO})} \left( E - \frac{q^2}{2m_N}, q \right) t_{q,t \rightarrow t}^{(L)}(E, k, q), \quad (17)$$

and

$$\begin{bmatrix} t_{d,t \rightarrow t}^{(L)} & t_{d,s_1 \rightarrow t}^{(L)} & t_{d,s_2 \rightarrow t}^{(L)} \\ t_{d,t \rightarrow s_1}^{(L)} & t_{d,s_1 \rightarrow s_1}^{(L)} & t_{d,s_2 \rightarrow s_1}^{(L)} \\ t_{d,t \rightarrow s_2}^{(L)} & t_{d,s_1 \rightarrow s_2}^{(L)} & t_{d,s_2 \rightarrow s_2}^{(L)} \end{bmatrix} (E, k, p) = \begin{Bmatrix} y_{tt} [K_s^{(L)} + K_c^{(L, \text{PC})} + \delta_0^L \frac{2H(\Lambda)}{\Lambda^2}] & -y_{ts} [K_s^{(L)} + \delta_0^L \frac{2H(\Lambda)}{3\Lambda^2}] & -y_{ts} [2K_s^{(L)} + \delta_0^L \frac{4H(\Lambda)}{3\Lambda^2}] \\ -y_{ts} [K_s^{(L)} + \delta_0^L \frac{2H(\Lambda)}{3\Lambda^2}] & -y_{ss} [\frac{K_s^{(L)}}{3} - \frac{K_c^{(L, \text{PC})}}{3} - \delta_0^L \frac{2H(\Lambda)}{9\Lambda^2}] & y_{ss} [\frac{2K_s^{(L)}}{3} + \delta_0^L \frac{4H(\Lambda)}{9\Lambda^2}] \\ -y_{ts} [2K_s^{(L)} + \delta_0^L \frac{4H(\Lambda)}{3\Lambda^2}] & y_{ss} [\frac{2K_s^{(L)}}{3} + \delta_0^L \frac{4H(\Lambda)}{9\Lambda^2}] & y_{ss} \delta_0^L \frac{8H(\Lambda)}{9\Lambda^2} \end{Bmatrix}$$

$$\begin{aligned}
 & + \frac{1}{2\pi^2} \int_0^\Lambda d q q^2 \left\{ \begin{array}{ccc} -y_{tt} [K_s^{(L)} + K_c^{(L),PC} + \delta_0^L \frac{2H(\Lambda)}{\Lambda^2}] & y_{ts} [3K_s^{(L)} + \delta_0^L \frac{2H(\Lambda)}{\Lambda^2}] & y_{ts} [3K_s^{(L)} + \delta_0^L \frac{2H(\Lambda)}{\Lambda^2}] \\ y_{ts} [K_s^{(L)} + \delta_0^L \frac{2H(\Lambda)}{3\Lambda^2}] & y_{ss} [K_s^{(L)} - K_c^{(L),PC} - \delta_0^L \frac{2H(\Lambda)}{3\Lambda^2}] & -y_{ss} [K_s^{(L)} + \delta_0^L \frac{2H(\Lambda)}{3\Lambda^2}] \\ y_{ts} [2K_s^{(L)} + \delta_0^L \frac{4H(\Lambda)}{3\Lambda^2}] & -y_{ss} [2K_s^{(L)} + \delta_0^L \frac{4H(\Lambda)}{3\Lambda^2}] & -y_{ss} \delta_0^L \frac{4H(\Lambda)}{3\Lambda^2} \end{array} \right\} \\
 & \times \mathcal{D}^{(LO)} \left( E - \frac{q^2}{2m_N}, q \right) \begin{bmatrix} t_{d,t \rightarrow t}^{(L)} & t_{d,s_1 \rightarrow t}^{(L)} & t_{d,s_2 \rightarrow t}^{(L)} \\ t_{d,t \rightarrow s_1}^{(L)} & t_{d,s_1 \rightarrow s_1}^{(L)} & t_{d,s_2 \rightarrow s_1}^{(L)} \\ t_{d,t \rightarrow s_2}^{(L)} & t_{d,s_1 \rightarrow s_2}^{(L)} & t_{d,s_2 \rightarrow s_2}^{(L)} \end{bmatrix} (E, k, q), \quad (18)
 \end{aligned}$$

where the subscripts  $q$  and  $d$  denote the quartet and doublet states, respectively. The subscripts  $t$ ,  $s_1$ , and  $s_2$  are for dibaryons in the triplet, singlet, and  $pp$  part of singlet states.  $K_s^{(L)}$  and  $K_c^{(L)}$  are the kernels with the strong and Coulomb interactions, respectively, with  $L$  denoting the scattering in the  $L$ -wave channel. The complete form of these kernels and the other symbols have been introduced in Ref. [5].

The  $\mathcal{D}^{(LO)}$  represents the matrix propagator of the dibaryon auxiliary fields as

$$\mathcal{D}^{(LO)}(E, q) = \begin{bmatrix} D_t^{(LO)}(E, q) & 0 & 0 \\ 0 & D_s^{(LO)}(E, q) & 0 \\ 0 & 0 & D_{s,pp}^{(LO)}(E, q) \end{bmatrix}, \quad (19)$$

where the LO propagators for the  ${}^3S_1$ ,  ${}^1S_0$ , and  $pp$  part of the  ${}^1S_0$  dibaryon are given by

$$\begin{aligned}
 D_{t/s}^{(LO)}(E, q) &= \frac{4\pi}{m_N y_{t/s}^2} \frac{1}{\gamma_{t/s} - \sqrt{\frac{q^2}{4} - m_N E - i\epsilon}}, \\
 D_{s,pp}^{(LO)}(E, q) &= \frac{4\pi}{m_N y_s^2} \frac{1}{\frac{1}{a_c} + \alpha m_N \tilde{H}_0\left(\frac{\alpha m_N}{2q'}\right)}, \quad (20)
 \end{aligned}$$

with

$$\alpha = \frac{e^2}{4\pi} \sim \frac{1}{137}, \quad q' = i\sqrt{\frac{q^2}{4} - m_N E - i\epsilon}, \quad (21)$$

$$\tilde{H}_0(\eta) = \psi(i\eta) + \frac{1}{2i\eta} - \log(i\eta). \quad (22)$$

In the above equation, the function  $\psi$  is the logarithmic derivative of the  $\Gamma$  function. Moreover,  $a_c$  denotes the scattering length in the  $pp$  channel.

#### IV. PV AMPLITUDE OF THE $pd \rightarrow {}^3\text{He}\gamma$ PROCESS

In this section, we focus on the PV amplitude of the  $pd \rightarrow {}^3\text{He}\gamma$  process. We concentrate in the region  $E_{\text{Lab}} \geq 0.5$  MeV because in this regime the Coulomb parameter  $\frac{\alpha m_N}{p}$  is of order  $\frac{1}{3}$ , and therefore the Coulomb effects can be treated perturbatively. We use the Lagrangian in Eq. (11) for the PV interaction to calculate the EM matrix elements that contribute in the  $pd \rightarrow {}^3\text{He}\gamma$  process at  $E_{\text{Lab}} \geq 0.5$  MeV.

For  $E_{\text{Lab}} \geq 0.5$  MeV, we must calculate the PV  $E1$  and  $M1$  transitions in the  $pd \rightarrow {}^3\text{He}\gamma$  process. The diagrams that contribute in the PV  $pd$  radiative capture are shown schematically in Figs. 2 and 3. The diagrams in Fig. 2 are the PC diagrams that multiplied by the PV scattering, and the diagrams

in Fig. 3 indicate the PV diagrams with the half-off-shell PC scattering. In Fig. 3 the dashed oval indicates the PC nucleon-dibaryon scattering amplitudes which are obtained using Eqs. (16) and (18) and the dashed half-oval is the normalized  ${}^3\text{He}$  wave function at LO which is denoted by  $t_{{}^3\text{He}}^{(LO)}$  as Ref. [5]. The dashed rectangular in Fig. 2 is the PV  $pd$ -scattering amplitude of diagrams shown in Fig. 1. The dashed rectangular with the dashed line around it in Fig. 3 represents the PV  $pd$  scattering depicted in Fig. 1 without participation of the diagrams which have the full PC  $pd$  scattering on the right-hand side.

The incoming  ${}^2S_{\frac{1}{2}}$  and  ${}^4S_{\frac{3}{2}}$  states of the proton-deuteron system can be changed to make the final  ${}^2S_{\frac{1}{2}}$   ${}^3\text{He}$  state using the combination of  $E1$  and PV interactions. Also, the mixing of  $M1$  and PV interactions can convert the initial  ${}^2P_{\frac{1}{2}}$ ,  ${}^2P_{\frac{3}{2}}$ ,  ${}^4P_{\frac{1}{2}}$ , and  ${}^4P_{\frac{3}{2}}$  channels of the proton-deuteron system to the final  ${}^3\text{He}$  ground state. So, we generally have two  $E1$  PV transitions,

$${}^2S_{\frac{1}{2}} \rightarrow {}^2S_{\frac{1}{2}}, \quad {}^4S_{\frac{3}{2}} \rightarrow {}^2S_{\frac{1}{2}}, \quad (23)$$

and four  $M1$  PV transitions which make the final  ${}^3\text{He}$  ground state

$$\begin{aligned}
 {}^2P_{\frac{1}{2}} &\rightarrow {}^2S_{\frac{1}{2}}, \quad {}^2P_{\frac{3}{2}} \rightarrow {}^2S_{\frac{1}{2}}, \\
 {}^4P_{\frac{1}{2}} &\rightarrow {}^2S_{\frac{1}{2}}, \quad {}^4P_{\frac{3}{2}} \rightarrow {}^2S_{\frac{1}{2}}. \quad (24)
 \end{aligned}$$

For the diagrams in Fig. 2, we have the PV  $E1$  and  $M1$  transitions as

$$\begin{aligned}
 X &\xrightarrow{\text{PV}} Y \xrightarrow{E1} {}^2S_{\frac{1}{2}}, \\
 Y &\xrightarrow{\text{PV}} X \xrightarrow{M1} {}^2S_{\frac{1}{2}}. \quad (25)
 \end{aligned}$$

With respect to the fact that the electric transition does not change the relative spin of particles and also the magnetic transition does not change the orbital angular momentum, all the  $E1$  and  $M1$  transitions which create the  ${}^2S_{\frac{1}{2}}$  state are

$$\begin{aligned}
 {}^2P_{\frac{1}{2}} &\xrightarrow{E1} {}^2S_{\frac{1}{2}}, \quad {}^2P_{\frac{3}{2}} \xrightarrow{E1} {}^2S_{\frac{1}{2}}, \\
 {}^2S_{\frac{1}{2}} &\xrightarrow{M1} {}^2S_{\frac{1}{2}}, \quad {}^4S_{\frac{3}{2}} \xrightarrow{M1} {}^2S_{\frac{1}{2}}. \quad (26)
 \end{aligned}$$

So, we finally have six possible transitions for the diagrams in Fig. 2 from the incoming  $S$  and  $P$  waves to the final  ${}^3\text{He}$  ground state as

$$\begin{aligned}
 {}^2S_{\frac{1}{2}} &\xrightarrow{\text{PV}} {}^2P_{\frac{1}{2}} \xrightarrow{E1} {}^2S_{\frac{1}{2}}, \quad {}^4S_{\frac{3}{2}} \xrightarrow{\text{PV}} {}^2P_{\frac{3}{2}} \xrightarrow{E1} {}^2S_{\frac{1}{2}}, \\
 {}^2P_{\frac{1}{2}} &\xrightarrow{\text{PV}} {}^2S_{\frac{1}{2}} \xrightarrow{M1} {}^2S_{\frac{1}{2}}, \quad {}^4P_{\frac{1}{2}} \xrightarrow{\text{PV}} {}^2S_{\frac{1}{2}} \xrightarrow{M1} {}^2S_{\frac{1}{2}}, \\
 {}^2P_{\frac{3}{2}} &\xrightarrow{\text{PV}} {}^4S_{\frac{3}{2}} \xrightarrow{M1} {}^2S_{\frac{1}{2}}, \quad {}^4P_{\frac{3}{2}} \xrightarrow{\text{PV}} {}^4S_{\frac{3}{2}} \xrightarrow{M1} {}^2S_{\frac{1}{2}}. \quad (27)
 \end{aligned}$$

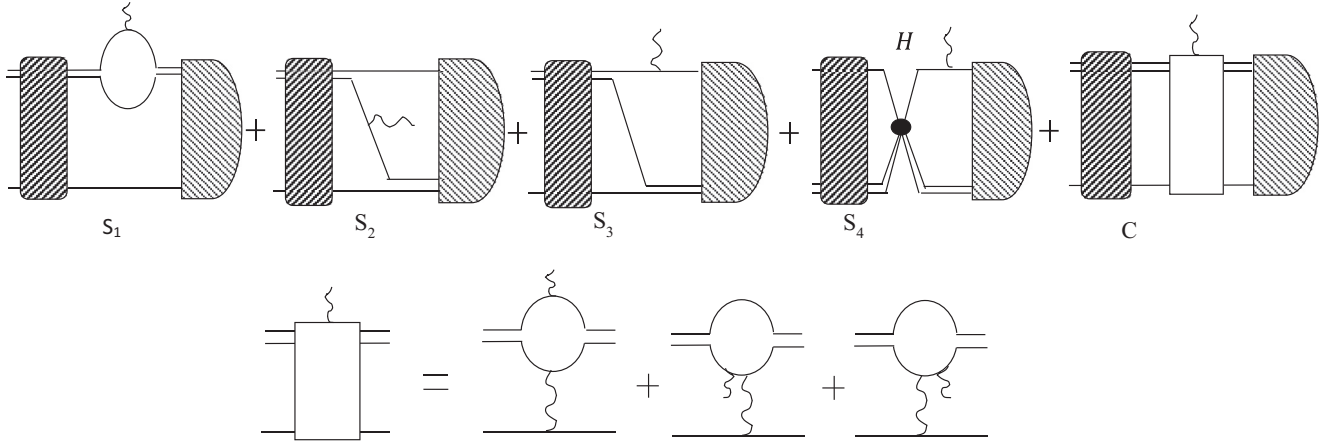


FIG. 2. The first set of the diagrams for the PV  $pd \rightarrow {}^3\text{He}\gamma$  process at LO. The dashed rectangular with solid line around it denotes the contribution of all PV  $pd$ -scattering diagrams depicted in Fig. 1. The  $C$  diagram indicates the Coulomb effect that only appears in the  $pd \rightarrow {}^3\text{He}\gamma$  transition. The dashed half-oval is the normalized  ${}^3\text{He}$  wave function at LO. The wavy line which exits from the nucleon denotes the emitted photon and  $H$  is the leading-order three-body force.

In order to calculate the diagrams in Fig. 2, we need six PV  $pd$ -scattering amplitudes,  $t^{\text{LO,PV}}(X/Y \rightarrow Y/X)$ , corresponding to the transitions in Eq. (27).

If we use this procedure for the diagrams in Fig. 3, then 10 possible transitions,

$$\begin{aligned} & {}^2S_{\frac{1}{2}} \xrightarrow{E_1} {}^2P_{\frac{1}{2}} \xrightarrow{\text{PV}} {}^2S_{\frac{1}{2}}, \quad {}^4S_{\frac{3}{2}} \xrightarrow{E_1} {}^4P_{\frac{1}{2}} \xrightarrow{\text{PV}} {}^2S_{\frac{1}{2}}, \\ & {}^2P_{\frac{1}{2}} \xrightarrow{M_1} {}^2P_{\frac{1}{2}} \xrightarrow{\text{PV}} {}^2S_{\frac{1}{2}}, \quad {}^4P_{\frac{1}{2}} \xrightarrow{M_1} {}^2P_{\frac{1}{2}} \xrightarrow{\text{PV}} {}^2S_{\frac{1}{2}}, \\ & {}^2P_{\frac{3}{2}} \xrightarrow{M_1} {}^2P_{\frac{1}{2}} \xrightarrow{\text{PV}} {}^2S_{\frac{1}{2}}, \quad {}^4P_{\frac{3}{2}} \xrightarrow{M_1} {}^2P_{\frac{1}{2}} \xrightarrow{\text{PV}} {}^2S_{\frac{1}{2}}, \\ & {}^2P_{\frac{1}{2}} \xrightarrow{M_1} {}^4P_{\frac{1}{2}} \xrightarrow{\text{PV}} {}^2S_{\frac{1}{2}}, \quad {}^2P_{\frac{3}{2}} \xrightarrow{M_1} {}^4P_{\frac{1}{2}} \xrightarrow{\text{PV}} {}^2S_{\frac{1}{2}}, \\ & {}^2P_{\frac{3}{2}} \xrightarrow{M_1} {}^4P_{\frac{1}{2}} \xrightarrow{\text{PV}} {}^2S_{\frac{1}{2}}, \quad {}^4P_{\frac{3}{2}} \xrightarrow{M_1} {}^4P_{\frac{1}{2}} \xrightarrow{\text{PV}} {}^2S_{\frac{1}{2}}, \end{aligned} \quad (28)$$

will be possible for PV proton capture on deuteron. Taking the transitions in Eq. (28) into the calculation, the dashed

rectangular with dashed line around it as noted by  $\tilde{t}^{\text{LO,PV}}(X/Y \rightarrow Y/X)$  should be considered for the appropriate incoming and outgoing channels.

So the PV amplitude for the  $pd \rightarrow {}^3\text{He}\gamma$  transition is obtained using the relation

$$W^{\text{PV}}(X/Y; E_i, k) = W_I^{\text{PV}}(X/Y; E_i, k) + W_{II}^{\text{PV}}(X/Y; E_i, k), \quad (29)$$

where  $W_I^{\text{PV}}(X/Y; E_i, k)$  and  $W_{II}^{\text{PV}}(X/Y; E_i, k)$  are the amplitudes of the first and second sets of the PV diagrams that shown in Figs. 2 and 3, respectively.

Now we initially introduce the evaluation of the diagrams in Fig. 2 and then explain about those of Fig. 3. In the cluster configuration space, the contribution of all diagrams in Fig. 2 for the incoming  $X/Y$  channel can be written as

$$W_I^{\text{PV}}(X/Y; E_i, k) = -\frac{1}{2\pi^2} \int_0^\Lambda dq q^2 \left[ \sum_{j=1}^4 S_j(Y/X; E_i, k) + C(Y/X; E_i, k) \right] \mathcal{D}^{(\text{LO})} \left( E_i - \frac{q^2}{2m_N}, q \right) t^{\text{LO,PV}}(X/Y \rightarrow Y/X; E_i, k, q), \quad (30)$$

where the  $S_j(X/Y; E_i, k)$  with  $j = 1, \dots, 4$  represents the contribution of the “ $S_j$ ” diagram in Fig. 2. The  $k$  is the incoming momentum,  $E_f = -B_{{}^3\text{He}}$  with  $B_{{}^3\text{He}}$  is the  ${}^3\text{He}$  binding energy, and  $E_i = E = \frac{3k^2}{4m_N} - \frac{Y_i^2}{m_N}$  indicates the center-of-mass (c.m.) energy of the incoming  $pd$  system. Also,  $C(X/Y; E_i, k)$  denotes the contribution of the diagram “ $C$ ”, which is constructed using the additional diagrams in the second line of Fig. 2. The detailed derivations of  $S_j(X/Y; E_i, k)$  and  $C(X/Y; E_i, k)$  functions have been presented in our previous paper [5].

For the incoming  $X/Y$  channel, the contribution of the diagrams in Fig. 3 can be written as

$$W_{II}^{\text{PV}}(X/Y; E_i, k) = R(X/Y; E_i, k) - \frac{1}{2\pi^2} \int_0^\Lambda dq q^2 R(X/Y; E_i, q) \mathcal{D}^{(\text{LO})} \left( E_i - \frac{q^2}{2M}, q \right) t^{\text{LO,PC}}(X/Y; E_i, k, q), \quad (31)$$

with

$$R(X/Y; E_i, k) = \sum_{j=1}^{30} R_j(X/Y; E_i, k), \quad (32)$$

where the  $3 \times 3$  matrix function  $R_j$  denotes the contribution of the diagram “ $R_j$ ” in Fig. 3. The detailed calculation for one of the most important diagrams,  $R_{16}$ , for all the incoming partial waves is depicted in Appendix.

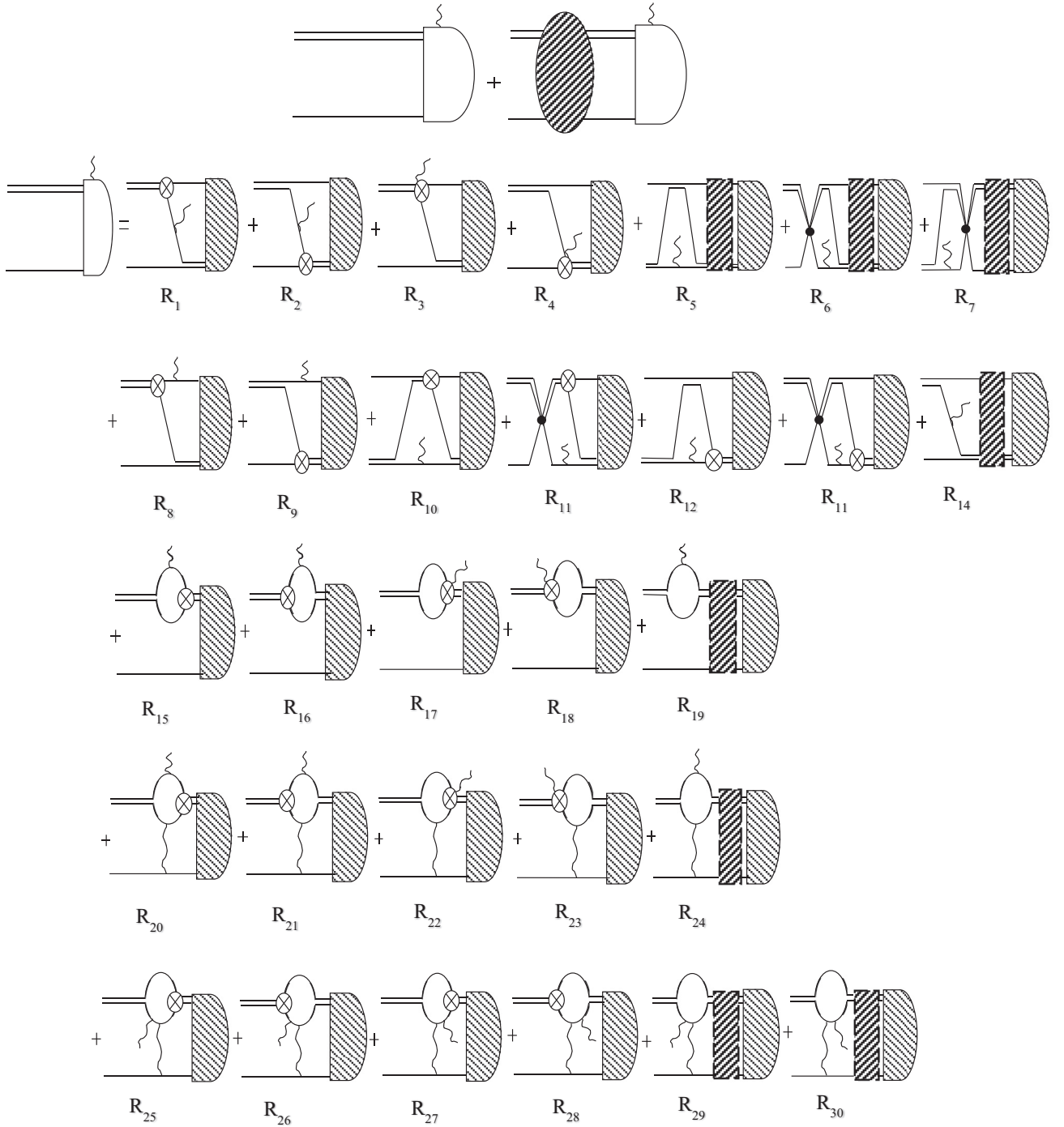


FIG. 3. The second set of the diagrams for the PV  $pd \rightarrow {}^3\text{He}\gamma$  process at LO. The circle with a cross and wavy line is the PV photon-baryon-nucleon-nucleon ( $\gamma dNN$ ) vertex. The dashed rectangular with dashed line around it denotes the PV  $pd$  scattering depicted in Fig. 1 without participation of the diagrams which have the full PC  $pd$  scattering on the right-hand side.

Finally, the physical amplitude of all diagrams in Figs. 2 and 3 can be written as

$$\mathcal{W}^{\text{PV}}(X/Y; E_i, k) = W^{\text{PV}}(X/Y; E_i, k) \begin{pmatrix} \sqrt{\mathcal{Z}^{\text{LO}}} \\ 0 \\ 0 \end{pmatrix}, \quad (33)$$

where  $\mathcal{Z}^{\text{LO}}$  is the normalization factor of the incoming deuteron wave function at LO [5].

## V. NUMERICAL RESULTS

To calculate the outgoing photon circular polarization in the  $pd \rightarrow {}^3\text{He}\gamma$  process, one needs the PC and PV amplitudes of the  $pd$  capture process. The detailed derivations of the LO PC calculations for the  $pd$ -scattering amplitude,  ${}^3\text{He}$  wave function, and, finally, the  $pd \rightarrow {}^3\text{He}\gamma$  transition amplitude have been previously presented in Ref. [5].

TABLE I. The PV observables which have been recently studied using the EFT( $\not{\epsilon}$ ) formalism. The available measured values of these observables are summarized in the third column.

Observables	EFT( $\not{\epsilon}$ ) relations	Experiment
$P_\gamma^{np}$ [3]	$[-28.699 g_1 + 14.024 (g_2 - 2 g_4)] \times 10^3$	$(1.8 \pm 1.8) \times 10^{-7}$ [23]
$A_\gamma^{np}$ [3]	$[4.102 g_5] \times 10^3$	$(-0.60 \pm 0.21) \times 10^{-7}$ [24]
$\frac{1}{\rho} \frac{d\Phi^{np}}{dl}$ [22]	$[4.5 (2g_5 + g_1) - 18.5 (g_2 - 2 g_4)] \text{ rad MeV}^{-2}$	$(-0.15 \pm 0.47) \times 10^{-7}$ [25]
$\frac{1}{\rho} \frac{d\Phi^{nd}}{dl}$ [22]	$[8.0 g_5 + 17.0 g_1 + 2.3(3g_2 - 2 g_3)] \text{ rad MeV}^{-2}$	
$P_\gamma^{nd}$ [4]	$[0.26 g_1 - 0.23 g_2 + 0.15 g_3 - 1.08 g_5] \times 10^3$	
$Q_\gamma^{nd}$ [26]	$[-0.51 g_1 + 0.83 g_2 - 0.47 g_3 + 1.36 g_5] \times 10^3$	
$A_\gamma^{nd}$ [26]	$[1.36 g_1 - 1.50 g_2 + 0.94 g_3 - 4.47 g_5] \times 10^3$	
$P_\gamma^{pd}$ (this work)	$[0.17 g_1 - 0.49 g_2 + 0.47 g_3 - 2.00 g_5] \times 10^3$	

The PV  $E1$  and  $M1$  transition amplitudes of the proton radiative capture on a deuteron are required to obtain the contributions of the diagrams in Figs. 2 and 3. In the previous section we derived the LO EFT( $\not{\epsilon}$ ) amplitudes of the diagrams presented as the first set in Fig. 2. The PV  $pd$ -scattering amplitude is an essential building block for the amplitudes of the first set of PV diagrams and has been fully derived in Ref. [18]. The contributions of the second set of the PV  $pd \rightarrow {}^3\text{He} \gamma$  diagrams which are shown in Fig. 3 can be obtained after evaluating the  $R(X/Y; E_i, k)$  matrix function. The final results of the second set of PV diagrams are given by adding the contribution of the half-off-shell PC  $pd$ -scattering amplitude multiplied by the  $R(X/Y; E_i, k)$  matrix element.

In order to compute the PC and PV amplitudes of the  $pd \rightarrow {}^3\text{He} \gamma$  process, we initially obtain the PC  $pd$ -scattering amplitude by solving numerically the Faddeev equations with

the Hetherington-Schick method [19–21] in a *Mathematica* code with an arbitrary cutoff momentum  $\Lambda$ . Also we obtain the PV  $pd$ -scattering amplitude of the diagrams in Fig. 1, with the same cutoff momentum  $\Lambda$  as used in the PC-scattering amplitude. In the last step, we calculate the contribution of the PC and PV amplitudes by solving numerically the loop-momentum integrations with the Gaussian quadrature weights and the same cutoff momentum as the other steps.

The photon circular polarization is given by

$$P_\gamma = \frac{\sigma_+ - \sigma_-}{\sigma_+ + \sigma_-}, \quad (34)$$

where  $\sigma_+$  and  $\sigma_-$  are the cross section for the photons with right and left helicity, respectively.

After summing over the spin and polarization of the proton and deuteron, we have

$$P_\gamma^{pd} = 2 \frac{\text{Re}[\sum_{U=1,3,5} W^{\text{PC}\dagger}(U) W^{\text{PV}}(U) + 2 \sum_{U=2,4,6} W^{\text{PC}\dagger}(U) W^{\text{PV}}(U)]}{\sum_{U=1,3,5} |W^{\text{PC}}(U)|^2 + 2 \sum_{U=2,4,6} |W^{\text{PC}}(U)|^2}, \quad (35)$$

with  $W^{\text{PC}}(U)$  and  $W^{\text{PV}}(U)$  as the PC and PV amplitudes of  $pd \rightarrow {}^3\text{He} \gamma$  process for the incoming channel  $U$ , where  $U = 1, \dots, 6$  are instead  ${}^2S_{1/2}$ ,  ${}^4S_{3/2}$ ,  ${}^2P_{1/2}$ ,  ${}^2P_{3/2}$ ,  ${}^4P_{1/2}$ , and  ${}^4P_{3/2}$ , respectively.

In order to obtain the exact EFT  $P_\gamma^{pd}$  value, the five PV LECs introduced in the Lagrangian (11) must be exactly determined. In other words, without the fixed values for the PV LECs, the final relations of any few-body observables are obtained as a function of these five unknown coupling constants. We expect the fact that the magnitude of the PV coupling constants to be of the order  $\sim 10^{-10} \text{ MeV}^{-\frac{3}{2}}$  [22]. This is an order-of-magnitude estimation and may be off by factors of 10 or more.

Here as an example, the calculated result for  $P_\gamma^{pd}$  at  $E_{\text{Lab}} = E_p = \frac{9k^2}{8m_N} = 2.048 \text{ MeV}$  is evaluated in terms of the PV LECs as

$$P_\gamma^{pd} = \left[ 0.17 g^{({}^3S_1-{}^1P_1)} - 0.49 g_{(\Delta I=0)}^{({}^1S_0-{}^3P_0)} + 0.47 g_{(\Delta I=1)}^{({}^1S_0-{}^3P_0)} - 2.00 g^{({}^3S_1-{}^3P_1)} \right] \times 10^3. \quad (36)$$

The Coulomb effect in the results of Eq. (36) can be investigated by switching off the Coulomb interaction in the final  $P_\gamma^{pd}$  result. The value of the outgoing circular polarization on the  $pd \rightarrow {}^3\text{He} \gamma$  process for  $E_{\text{Lab}} = 2.048 \text{ MeV}$  without any Coulomb interaction is calculated as

$$P_\gamma^{pd} = \left[ 0.20 g^{({}^3S_1-{}^1P_1)} - 0.60 g_{(\Delta I=0)}^{({}^1S_0-{}^3P_0)} + 0.58 g_{(\Delta I=1)}^{({}^1S_0-{}^3P_0)} - 2.21 g^{({}^3S_1-{}^3P_1)} \right] \times 10^3. \quad (37)$$

The above results indicate that the Coulomb interaction introduces some corrections, about 10–20%, in the coefficients of the PV LECs. These small Coulomb effects rely on the perturbative Coulomb corrections at the  $k \sim 40 \text{ MeV}$  corresponding to  $E_{\text{Lab}} = 2.048 \text{ MeV}$  as we expected from the power counting introduced in Sec. II B. We can see from the coefficients of  $g^{(\bar{x}-\bar{y})}$  in Eqs. (36) and (38) that the dominant contribution comes from the  $g^{({}^3S_1-{}^3P_1)}$  LEC.

By considering the estimated values of the PV coupling constants of the order  $\sim 10^{-10} \text{ MeV}^{-\frac{3}{2}}$ , the values of  $P_\gamma^{pd}$  in

TABLE II. The determined values of the PV coupling constants  $g^{(\bar{x}-\bar{y})}$ . The PV coupling constants values in the second and third rows are the estimations based on the evaluation by Moeini Arani [26] and the extraction from Vanasse [27], respectively. All values are in units of  $\text{MeV}^{-\frac{3}{2}}$ .

$g^{(3S_1-1P_1)}$	$g_{(\Delta I=0)}^{(1S_0-3P_0)}$	$g_{(\Delta I=1)}^{(1S_0-3P_0)}$	$g_{(\Delta I=2)}^{(1S_0-3P_0)}$	$g^{(3S_1-3P_1)}$
$2.78 \times 10^{-12}$	$4.71 \times 10^{-9}$	$2.41 \times 10^{-9}$	$2.35 \times 10^{-9}$	$1.29 \times 10^{-11}$
$9.88 \times 10^{-12}$	$6.81 \times 10^{-12}$	$6.67 \times 10^{-13}$	$1.99 \times 10^{-12}$	$3.63 \times 10^{-11}$

Eqs. (36) and (38) are estimated as

$$|P_\gamma^{pd}| \sim 10^{-6} - 10^{-7}. \quad (38)$$

In the past years, the EFT( $\not{\tau}$ ) formalism has been applied to study the parity violation in the two- and three-body systems. We present the relations for the PV observables on the few-body systems which have been investigated with the EFT( $\not{\tau}$ ) approach in terms of PV LECs in the Table I. As shown in the third column of Table I, the values of the photon asymmetry with respect to the neutron polarization  $A_\gamma^{np}$  and the circular polarization of the outgoing photon on  $np \rightarrow d\gamma$   $P_\gamma^{np}$  have been previously reported. The uncertainties of these measurements denote that the available experimental data are not accurate. There are no experimental data on the neutron-proton spin rotation  $\frac{d\Phi^{np}}{dl}$  and the neutron-deuteron spin rotation  $\frac{d\Phi^{nd}}{dl}$ . The experimental data for the circular polarization of  $\gamma$  emission  $P_\gamma^{nd}$  and the asymmetry of the outgoing photon with respect to the neutron (deuteron) polarization  $a_\gamma^{nd}$  ( $A_\gamma^{nd}$ ) on the  $nd \rightarrow {}^3\text{He}\gamma$  have not been reported to this point. In order to determine PV LECs, we need to increase the accuracy of existing measurements and to introduce new experiments for measuring the neutron spin rotation on a variety of targets, the circular photon polarizations for the unpolarized beam (neutron or proton) and target (deuteron), and the polarized photon induced processes on the deuteron, triton, and helium.

In the present circumstance with no available experimental data Moeini Arani and Bayegan have introduced the PV

TABLE III. The results for the photon circular polarization of the  $pd \rightarrow {}^3\text{He}\gamma$  at LO are shown at the energy  $0.5 \leq E_{\text{Lab}} \leq 3$  MeV with  $\Lambda = 600$ . The results in the second and third columns are obtained based on the set of the  $g^{(\bar{x}-\bar{y})}$  estimated in Refs. [26] and [27], respectively. The numbers in the parentheses in the second column indicate the results for  $P_\gamma^{pd}$  when the Coulomb effect is switched off. These results are presented in units of  $10^{-6}$ .

$E_{\text{Lab}}(\text{MeV})$	$P_\gamma^{pd}$	
	Based on Ref. [26]	Based on Ref [27]
0.57	-2.80 (-3.02)	0.23
0.80	-2.10 (-2.32)	0.16
1.12	-1.68 (-1.90)	0.12
1.53	-1.40 (-1.64)	0.09
2.04	-1.21 (-1.47)	0.07
2.65	-0.94 (-1.10)	0.05
3.00	-1.09 (-1.37)	0.04

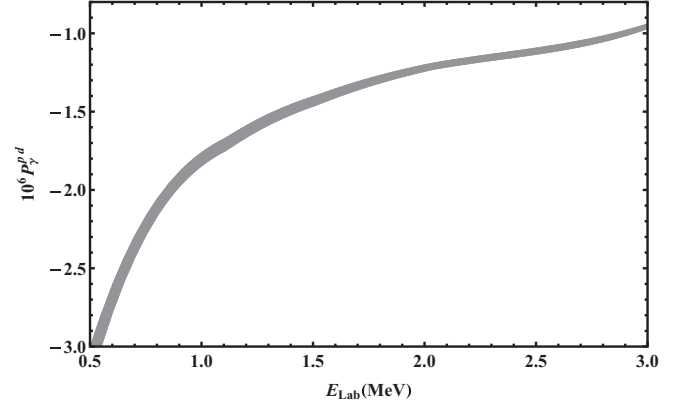


FIG. 4. Variation of the  $P_\gamma^{pd}$  according to the proton laboratory energies from 0.5 to 3 MeV between  $\Lambda = 400$  and 900 MeV based on the  $g^{(\bar{x}-\bar{y})}$  presented in the second row of Table II.

coefficients values by matching the five EFT( $\not{\tau}$ ) relations for the PV observables  $A_\gamma^{np}$ ,  $P_\gamma^{np}$ ,  $\frac{1}{\rho} \frac{d\Phi^{np}}{dl}$ ,  $\frac{1}{\rho} \frac{d\Phi^{nd}}{dl}$ , and  $P_\gamma^{nd}$  to the DDH “best values” estimates for these observables [26]. Vanasse has also obtained a different values for five PV LECs  $g^{(\bar{x}-\bar{y})}$  [27]. These two estimated values for the  $g^{(\bar{x}-\bar{y})}$  are shown in Table II.

According to the values of the PV coupling constants  $g^{(\bar{x}-\bar{y})}$  presented in Table II, we obtain the  $P_\gamma^{pd}$  for the energy values in the  $E_{\text{Lab}} \geq 0.5$  MeV region. Our evaluated results are depicted in Table III where the numbers in the parentheses in the second column indicate the results for  $P_\gamma^{pd}$  when the Coulomb effect is switched off. We have also presented the  $P_\gamma^{pd}$  values based on the  $g^{(\bar{x}-\bar{y})}$  extracted from Ref. [27] in the third column of Table III. The difference between the values of  $P_\gamma^{pd}$  according to two different values of the PV coupling constants in Refs. [26,27] can be assessed by the future experimental data.

The variation of the  $P_\gamma^{pd}$  at the proton laboratory energies from 0.5 to 3 MeV based on the  $g^{(\bar{x}-\bar{y})}$  values in the second row of Table II has been presented in Fig. 4. The thickness of the plot indicates the cutoff variation, which runs from 400 to 900 MeV. The results of the cutoff variation for  $P_\gamma^{pd}$  between  $\Lambda = 400$  and 900 MeV based on the  $g^{(\bar{x}-\bar{y})}$  in the second row of Table II are also shown in Table IV. We emphasize that the photon circular polarization in the  $pd \rightarrow {}^3\text{He}\gamma$  transition is not experimentally reported up to now. The other theoretical efforts have not been experimentally confirmed yet. However, we can see the order of our EFT( $\not{\tau}$ ) results agrees with the order of other electroweak observables for the few-body systems.

TABLE IV. The results for the cutoff variation of  $P_\gamma^{pd}$  between  $\Lambda = 400$  and 900 MeV based on the PV coupling constants indicated in Table II.

$E_{\text{Lab}}(\text{MeV})$	0.57	0.80	1.12	1.53	2.04	2.65	3.00
$\text{Abs}[1 - \frac{P_\gamma^{pd}(\Lambda=400)}{P_\gamma^{pd}(\Lambda=900)}]$	0.066	0.050	0.045	0.038	0.037	0.035	0.030

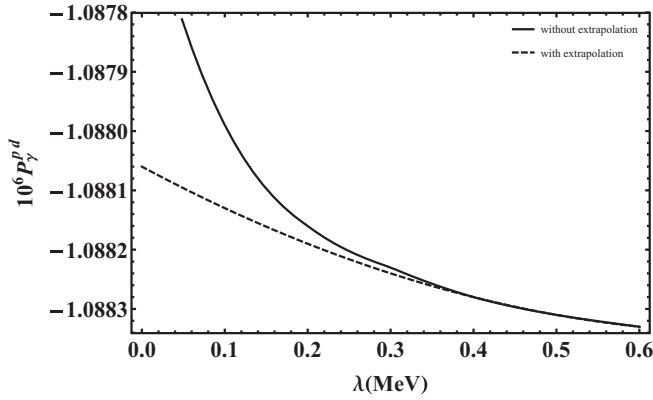


FIG. 5. The variation of the  $P_Y^{pd}$  according to photon mass for the proton laboratory energy of 2.65 MeV with  $\Lambda = 600$  MeV based on the values of five PV LECs in the second row of Table II. Dashed line represents the results with extrapolating and the solid line indicates the results without the extrapolation method.

In Sec. II B, the exchanged-photon propagator has been considered with a small photon mass to regulate the infrared divergences occurred within the integrations over the loop momenta. To obtain the physical results, we have to calculate the correct values when the photon mass goes to zero. For this purpose, we use the extrapolating method to find our results when  $\lambda \rightarrow 0$ . Figure 5 represents the comparison between the results of  $P_Y^{pd}$  according to the photon mass at the proton laboratory energy of 2.65 MeV with  $\Lambda = 600$  MeV. Dashed line represents the results with the extrapolation and the solid line indicates the results without any extrapolating in the final results. The results without using the extrapolating method grow up rapidly when the photon mass goes to zero because of the infrared divergences. We generally consider the function  $F(x) = \sum_{n=0}^{\infty} a_n x^n$  to interpolate the results of the  $P_Y^{pd}$  from  $\lambda = 0.4$  to  $0.6$  MeV. Despite the fact that the exact values of

$P_Y^{pd}$  for  $0.4 \leq \lambda \leq 0.6$  MeV behave nearly linear, the best fit to these results is obtained using the functional form of  $f(\lambda) = a_0 + a_1\lambda + a_2\lambda^2$  to extract the physical  $P_Y^{pd}$  value at  $\lambda = 0$ . The error introduced by the extrapolation to  $\lambda \rightarrow 0$  compared to the EFT theoretical error is negligible.

## VI. CONCLUSION AND OUTLOOK

Taking into account the appropriate effective Lagrangian which constructed by  $\mathcal{L}_s$ ,  $\mathcal{L}_{ph}$ ,  $\mathcal{L}_{EM}$ , and  $\mathcal{L}_{PV}$ , the photon circular polarization is accurately introduced in terms of the PV LECs for the  $pd \rightarrow {}^3\text{He}\gamma$  reaction. The observable comes from the interferences among weak, strong short-range, Coulomb long-range, and electromagnetic interactions in the  $0.5 \leq E_{\text{Lab}} \leq 3$  MeV energy region. The values of these LECs must be extracted from reliable experiments or QCD lattice calculations. In order to understand the complexity of PV in heavy nuclei, the five PV LECs will have to be determined and the model-independent EFT( $\tau$ ) nonleptonic weak interaction calculations to be reliably tested in few-nucleon systems.

### APPENDIX: THE CONTRIBUTION OF THE $R_{16}$ AMPLITUDE OF THE SECOND PV SET DIAGRAMS

One of the important diagrams in Fig. 3 is the diagram  $R_{16}$ . So, as an example, we introduce the derivations of the amplitude of the diagram  $R_{16}(U; E_i, k)$ , where  $U$  is the incoming channel ( $U = 1, \dots, 6$ ). The  $E_i$  and  $k$  are the same as the text. The contribution of all other diagrams are calculated with the same procedure and we do not report them here. The final results for the  $E1$  and  $M1$  transitions are obtained after applying the appropriate projection operators as Ref. [22] for the initial and final states.

#### 1. $E1$ transition

The amplitude of the diagram  $R_{16}$  in Fig. 3 before projecting to the arbitrary incoming and outgoing channels is obtained as

$$r_{16}^{(E1)}(E_i, k) = \frac{e y_i}{2m_N} t_{\text{He}}^{(LO)\dagger}(k) \mathcal{D}^{(LO)}\left(E_f - \frac{k^2}{2m_N}, k\right) \int \frac{d^4 q}{(2\pi)^4} \frac{1}{q_0 - \frac{q^2}{2m_N} + i\epsilon} \frac{1}{E_i - \frac{k^2}{2m_N} - q_0 - \frac{(k+q)^2}{2m_N} + i\epsilon} \\ \times \frac{1}{E_f - \frac{k^2}{2m_N} - q_0 - \frac{(k+q)^2}{2m_N} + i\epsilon} (\vec{k} + \vec{q}) \cdot \varepsilon_Y^* \begin{bmatrix} \frac{-2i}{\sqrt{2}} g_5 \varepsilon^{imj} (\vec{k} + 2\vec{q})_m & \frac{-2}{\sqrt{2}} g_2 \delta_3^A (\vec{k} + 2\vec{q})_j & \frac{-2}{\sqrt{2}} g_2 \delta_3^A (\vec{k} + 2\vec{q})_j \\ \frac{-1}{\sqrt{2}} g_1 \delta_3^B (\vec{k} + 2\vec{q})_i & 0 & 0 \\ \frac{-1}{\sqrt{2}} g_1 \delta_3^B (\vec{k} + 2\vec{q})_i & 0 & 0 \end{bmatrix}, \quad (\text{A1})$$

where the indices  $i, j, m$  are related to the initial, final, and intermediate spin states and indices  $A$  and  $B$  are related to the initial and final isospin states in the PV Lagrangian. It is necessary to know the pole positions of Eq. (A1) in the complex plane. So, we have three following poles

$$q_0 = \frac{q^2}{2m_N} - i\epsilon, \quad q_0 = E_i - \frac{k^2}{m_N} - \frac{q^2}{2m_N} - \frac{\vec{k} \cdot \vec{q}}{m_N} + i\epsilon, \quad q_0 = E_f - \frac{k^2}{m_N} - \frac{q^2}{2m_N} - \frac{\vec{k} \cdot \vec{q}}{m_N} + i\epsilon, \quad (\text{A2})$$

obtained from being zero the denominator of the nucleon propagators. With respect to the poles in Eq. (A2) and doing the integration over energy, the  $r_{16}^{(E1)}(E_i, k)$  becomes

$$\begin{aligned}
 r_{16}^{(E1)}(E_i, k) &= \frac{-ey_i}{8\sqrt{2}\pi^2(E_f - E_i)} t_{3\text{He}}^{(\text{LO})\dagger}(k) \mathcal{D}^{(\text{LO})}\left(E_f - \frac{k^2}{2m_N}, k\right) \int_0^\Lambda q^2 dq \int_{-1}^1 d(\cos\theta) \\
 &\times \left( \frac{1}{m_N E_i - k^2 - q^2 - \vec{k} \cdot \vec{q}} - \frac{1}{m_N E_f - k^2 - q^2 - \vec{k} \cdot \vec{q}} \right) (\vec{k} + \vec{q}) \cdot \varepsilon_\gamma^* \\
 &\times \begin{bmatrix} 2ig_5 \varepsilon^{imj} (\vec{k} + 2\vec{q})_m & 2g_2 \delta_3^A (\vec{k} + 2\vec{q})_j & 2g_2 \delta_3^A (\vec{k} + 2\vec{q})_j \\ g_1 \delta_3^B (\vec{k} + 2\vec{q})_i & 0 & 0 \\ g_1 \delta_3^B (\vec{k} + 2\vec{q})_i & 0 & 0 \end{bmatrix}. \tag{A3}
 \end{aligned}$$

The projected  $E1$  amplitude of the diagram  $R_{16}$  for the initial  ${}^2S_{1/2}$  state, in the cluster-configuration space, is given by

$$\begin{aligned}
 R_{16}({}^2S_{1/2}; E_i, k) &= \frac{ey_i}{24\sqrt{2}\pi^2(E_f - E_i)} t_{3\text{He}}^{(\text{LO})\dagger}(k) \mathcal{D}^{(\text{LO})}\left(E_f - \frac{k^2}{2m_N}, k\right) \int_0^\Lambda q^2 dq \int_{-1}^1 d(\cos\theta) \\
 &\times \left[ \frac{(\vec{k} + \vec{q}) \cdot (\vec{k} + 2\vec{q})}{m_N E_i - k^2 - q^2 - \vec{k} \cdot \vec{q}} - \frac{(\vec{k} + \vec{q}) \cdot (\vec{k} + 2\vec{q})}{m_N E_f - k^2 - q^2 - \vec{k} \cdot \vec{q}} \right] \\
 &\times \begin{pmatrix} 4g_5 & -2g_2 & 0 \\ -g_1 & 0 & 0 \\ 0 & 0 & 0 \end{pmatrix} t^\dagger [\vec{\varepsilon}_d \cdot \vec{\varepsilon}_\gamma^* + i\vec{\sigma} \cdot \vec{\varepsilon}_d \times \vec{\varepsilon}_\gamma^*] N. \tag{A4}
 \end{aligned}$$

Also, for the initial  ${}^4S_{3/2}$  state, the contribution of this diagram is given by

$$\begin{aligned}
 R_{16}({}^4S_{3/2}; E_i, k) &= \frac{ey_i}{24\sqrt{6}\pi^2(E_f - E_i)} t_{3\text{He}}^{(\text{LO})\dagger}(k) \mathcal{D}^{(\text{LO})}\left(E_f - \frac{k^2}{2M}, k\right) \int_0^\Lambda q^2 dq \int_{-1}^1 d(\cos\theta) \\
 &\times \left[ \frac{(\vec{k} + \vec{q}) \cdot (\vec{k} + 2\vec{q})}{m_N E_i - k^2 - q^2 - \vec{k} \cdot \vec{q}} - \frac{(\vec{k} + \vec{q}) \cdot (\vec{k} + 2\vec{q})}{m_N E_f - k^2 - q^2 - \vec{k} \cdot \vec{q}} \right] \\
 &\times \begin{pmatrix} -2g_5 & 0 & 0 \\ -g_1 & 0 & 0 \\ 0 & 0 & 0 \end{pmatrix} t^\dagger [2\vec{\varepsilon}_d \cdot \vec{\varepsilon}_\gamma^* - i\vec{\sigma} \cdot \vec{\varepsilon}_d \times \vec{\varepsilon}_\gamma^*] N. \tag{A5}
 \end{aligned}$$

## 2. M1 transition

In this section, we calculate the contribution of the  $M1$  transition of the diagram  $R_{16}$  as we have done in the previous section. The unprojected  $M1$  amplitude of the diagram  $R_{16}$  is evaluated using the relation

$$\begin{aligned}
 r_{16}^{(M1)}(E_i, k) &= \frac{ey_i}{2m_N} t_{3\text{He}}^{(\text{LO})\dagger}(k) \mathcal{D}^{(\text{LO})}\left(E_f - \frac{k^2}{2m_N}, k\right) \int \frac{d^4q}{(2\pi)^4} \frac{1}{q_0 - \frac{q^2}{2m_N} + i\epsilon} \frac{1}{m_N E_i - \frac{k^2}{2m_N} - q_0 - \frac{(k+q)^2}{2m_N} + i\epsilon} \\
 &\times \frac{1}{E_f - \frac{k^2}{2m_N} - q_0 - \frac{(k+q)^2}{2m_N} + i\epsilon} \begin{pmatrix} s_{11} & s_{12} & s_{13} \\ s_{21} & s_{22} & s_{23} \\ s_{31} & s_{32} & s_{33} \end{pmatrix}, \tag{A6}
 \end{aligned}$$

where

$$\begin{aligned}
 s_{11} &= \frac{1}{\sqrt{2}} [-2g_1 k_0 (\vec{k} + 2\vec{q})_i (B_j - 2B_2 \delta_2^j) + ig_5 k_1 (\vec{k} + 2\vec{q})_m \varepsilon^{imn} (2i \sum_n \varepsilon_{kjin} B_k - 2B_2 \delta_2^j)], \\
 s_{12} = s_{13} &= \frac{1}{\sqrt{2}} [2ig^2 (\vec{k} + 2\vec{q})_i k_1 \delta_3^A (\varepsilon_{kji} B_k - 2\varepsilon_{2ji} B_2)], \\
 s_{21} = s_{31} &= \frac{1}{\sqrt{2}} [-ig_5 k_1 \delta_3^B \varepsilon_{imn} (\vec{k} + 2\vec{q})_m (2\delta_n^k - 4\delta_2^n \delta_2^k) B_k], \\
 s_{22} = s_{23} = s_{32} = s_{33} &= \frac{1}{2\sqrt{2}} [-g_2 (\vec{k} + 2\vec{q})_i (2k_0 \delta_A^B - 2ik_1 \varepsilon_{3BA}) (2\delta_i^k - 4\delta_2^i \delta_2^k) \\
 &\quad - ig_3 (\vec{k} + 2\vec{q})_i (2\delta_i^k - 4\delta_2^i \delta_2^k) (-2k_0 \varepsilon_{AB3} - 2ik_1 \delta_3^A \delta_3^B + 2ik_1 \delta_A^B)]. \tag{A7}
 \end{aligned}$$

Here, we have the same poles as Eq. (A2). So, after doing the integration over energy, the obtained relation is

$$r_{16}^{(M1)}(E_i, k) = \frac{ey_t}{8\pi^2(E_f - E_i)} t_{\text{He}}^{(\text{LO})\dagger}(k) \mathcal{D}^{(\text{LO})}\left(E_f - \frac{k^2}{2m_N}, k\right) \int_0^\Lambda q^2 dq \int_{-1}^1 (d \cos \theta) \\ \times \left( \frac{1}{m_N E_i - k^2 - q^2 - \vec{k} \cdot \vec{q}} - \frac{1}{m_N E_f - k^2 - q^2 - \vec{k} \cdot \vec{q}} \right) \begin{pmatrix} s_{11} & s_{12} & s_{13} \\ s_{21} & s_{22} & s_{23} \\ s_{31} & s_{32} & s_{33} \end{pmatrix}. \quad (\text{A8})$$

For the initial  ${}^2P_{\frac{1}{2}}$ ,  ${}^4P_{\frac{1}{2}}$ ,  ${}^2P_{\frac{3}{2}}$ ,  ${}^4P_{\frac{3}{2}}$  states, in the cluster-configuration space, we obtain respectively:

$$R_{16}({}^2P_{\frac{1}{2}}; E_i, k) = \frac{-ey_t}{12\sqrt{2}\pi^2 k(E_f - E_i)} t_{\text{He}}^{(\text{LO})\dagger}(k) \mathcal{D}^{(\text{LO})}\left(E_f - \frac{k^2}{2m_N}, k\right) \int_0^\Lambda q^2 dq \int_{-1}^1 (d \cos \theta) \\ \times \left[ \frac{\vec{k} \cdot (\vec{k} + 2\vec{q})}{m_N E_i - k^2 - q^2 - \vec{k} \cdot \vec{q}} - \frac{\vec{k} \cdot (\vec{k} + 2\vec{q})}{m_N E_f - k^2 - q^2 - \vec{k} \cdot \vec{q}} \right] \\ \times \begin{pmatrix} 3k_0 g_1 + 4k_1 g_5 & 2g_2 k_1 & 0 \\ 2g_2 k_1 & g_2 k_0 & 0 \\ 0 & 0 & 2(g_2 k_1 - g_3 k_0) \end{pmatrix} t^\dagger [\vec{\varepsilon}_d \cdot \vec{\varepsilon}_\gamma^* + i\vec{\sigma} \cdot \vec{\varepsilon}_d \times \vec{\varepsilon}_\gamma^*] N, \quad (\text{A9})$$

$$R_{16}({}^2P_{\frac{3}{2}}; E_i, k) = \frac{-\sqrt{3}ey_t}{36\sqrt{2}\pi^2 k(E_f - E_i)} t_{\text{He}}^{(\text{LO})\dagger}(k) \mathcal{D}^{(\text{LO})}\left(E_f - \frac{k^2}{2m_N}, k\right) \int_0^\Lambda q^2 dq \int_{-1}^1 (d \cos \theta) \\ \times \left[ \frac{\vec{k} \cdot (\vec{k} + 2\vec{q})}{m_N E_i - k^2 - q^2 - \vec{k} \cdot \vec{q}} - \frac{\vec{k} \cdot (\vec{k} + 2\vec{q})}{m_N E_f - k^2 - q^2 - \vec{k} \cdot \vec{q}} \right] \\ \times \begin{pmatrix} k_1 g_5 & -g_2 k_1 & 0 \\ g_5 k_0 & g_2 k_0 & 0 \\ 0 & 0 & 2(k_0 + k_1)(g_2 - g_3) \end{pmatrix} t^\dagger [2\vec{\varepsilon}_d \cdot \vec{\varepsilon}_\gamma^* - i\vec{\sigma} \cdot \vec{\varepsilon}_d \times \vec{\varepsilon}_\gamma^*] N, \quad (\text{A10})$$

$$R_{16}({}^4P_{\frac{1}{2}}; E_i, k) = \frac{-ey_t}{12\pi^2 k(E_f - E_i)} t_{\text{He}}^{(\text{LO})\dagger}(k) \mathcal{D}^{(\text{LO})}\left(E_f - \frac{k^2}{2m_N}, k\right) \int_0^\Lambda q^2 dq \int_{-1}^1 (d \cos \theta) \\ \times \left[ \frac{\vec{k} \cdot (\vec{k} + 2\vec{q})}{m_N E_i - k^2 - q^2 - \vec{k} \cdot \vec{q}} - \frac{\vec{k} \cdot (\vec{k} + 2\vec{q})}{m_N E_f - k^2 - q^2 - \vec{k} \cdot \vec{q}} \right] \\ \times \begin{pmatrix} 2g_5 k_1 & 0 & 0 \\ g_5 k_0 & 0 & 0 \\ 0 & 0 & 0 \end{pmatrix} t^\dagger [\vec{\varepsilon}_d \cdot \vec{\varepsilon}_\gamma^* + i\vec{\sigma} \cdot \vec{\varepsilon}_d \times \vec{\varepsilon}_\gamma^*] N, \quad (\text{A11})$$

$$R_{16}({}^4P_{\frac{3}{2}}; E_i, k) = \frac{5ey_t}{12\sqrt{30}\pi^2 k(E_f - E_i)} t_{\text{He}}^{(\text{LO})\dagger}(k) \mathcal{D}^{(\text{LO})}\left(E_f - \frac{k^2}{2m_N}, k\right) \int_0^\Lambda q^2 dq \int_{-1}^1 (d \cos \theta) \\ \times \left[ \frac{\vec{k} \cdot (\vec{k} + 2\vec{q})}{m_N E_i - k^2 - q^2 - \vec{k} \cdot \vec{q}} - \frac{\vec{k} \cdot (\vec{k} + 2\vec{q})}{m_N E_f - k^2 - q^2 - \vec{k} \cdot \vec{q}} \right] \\ \times \begin{pmatrix} k_1 g_5 & 0 & 0 \\ 0 & 0 & 0 \\ 0 & 0 & 0 \end{pmatrix} t^\dagger [2\vec{\varepsilon}_d \cdot \vec{\varepsilon}_\gamma^* - i\vec{\sigma} \cdot \vec{\varepsilon}_d \times \vec{\varepsilon}_\gamma^*] N. \quad (\text{A12})$$

- [1] J. Erler and M. J. Ramsey-Musolf, *Prog. Part. Nucl. Phys.* **54**, 351 (2005).  
 [2] J. W. Shin, S. Ando, and C. H. Hyun, *Phys. Rev. C* **81**, 055501 (2010).  
 [3] M. R. Schindler and R. P. Springer, *Nucl. Phys. A* **846**, 51 (2010).

- [4] M. M. Arani and S. Bayegan, *Euro. Phys. J. A* **49**, 117 (2013).  
 [5] H. Nematollahi, S. Bayegan, N. Mahboubi, and M. M. Arani, *Phys. Rev. C* **94**, 054004 (2016).  
 [6] M. M. Arani, H. Nematollahi, N. Mahboubi, and S. Bayegan, *Phys. Rev. C* **89**, 064005 (2014).

- [7] M. R. Schindler and R. P. Springer, *Prog. Part. Nucl. Phys.* **72**, 1 (2013).
- [8] M. W. Ahmed, A. E. Champagne, B. R. Holstein, C. R. Howell, W. M. Snow, R. P. Springer, and W. K. Wu, *Proceedings, Community Summer Study 2013: Snowmass on the Mississippi (CSSS2013) Minneapolis, USA*, 2013.
- [9] H. W. Griesshammer, *Nucl. Phys. A* **744**, 192 (2004).
- [10] D. R. Phillips, G. Rupak, and M. J. Savage, *Phys. Lett. B* **473**, 209 (2000).
- [11] S. König and H.-W. Hammer, *Phys. Rev. C* **83**, 064001 (2011).
- [12] S. König, H. W. Griesshammer, and H.-W. Hammer, *J. Phys. G: Nucl. Part. Phys.* **42**, 045101 (2015).
- [13] G. Rupak and X. Kong, *Nucl. Phys. A* **717**, 73 (2003).
- [14] S. Ando and M. Brise, *J. Phys. G: Nucl. Part. Phys.* **37**, 105108 (2010).
- [15] F. Goeckner, W. K. Pitts, and L. D. Knutson, *Phys. Rev. C* **45**, R2536(R) (1992).
- [16] M. K. Smith and L. D. Knutson, *Phys. Rev. Lett.* **82**, 4591 (1999).
- [17] S. I. Ando, and Ch. H. Hyun, *Phys. Rev. C* **72**, 014008 (2005).
- [18] N. Mahboubi, S. Bayegan, H. Nematollahi, and M. M. Arani, *Phys. Rev. C* **94**, 054003 (2016).
- [19] J. H. Hetherington and L. H. Schick, *Phys. Rev.* **137**, B935 (1965).
- [20] R. T. Cahill and I. H. Sloan, *Nucl. Phys. A* **165**, 161 (1971).
- [21] R. Aaron and R. D. Amado, *Phys. Rev.* **150**, 857 (1966).
- [22] H. W. Griesshammer, M. R. Schindler, and R. P. Springer, *Eur. Phys. J. A* **48**, 7 (2012).
- [23] V. A. Knyazkov *et al.*, *Nucl. Phys. A* **417**, 209 (1984).
- [24] J. F. Cavaignac, B. Vignon, and R. Wilson, *Phys. Lett. B* **67**, 148 (1977).
- [25] J. Alberi *et al.*, *Can. J. Phys.* **66**, 542 (1988).
- [26] M. M. Arani and S. Bayegan, *Few-Body Syst.* **55**, 1099 (2014).
- [27] J. Vanasse, *Phys. Rev. C* **86**, 014001 (2012).